PHYSICAL REVIEW APPLIED **19,** 024008 (2023)

Three-Dimensional Mechanistic Modeling of Time-Dependent Dielectric Breakdown in Polycrystalline Thin Films

Qingqing Zhang,[1] Lishuai Yu,[1] Zhengpin Bian,[1] Dong Yuan,[1] Hailing Sun,[1] Biao Tang,[1]
Xubing Lu,[3] Feilong Liu,[1,*] and Guofu Zhou[1,2,†]

[1] *Guangdong Provincial Key Laboratory of Optical Information Materials and Technology & Institute of Electronic Paper Displays, South China Academy of Advanced Optoelectronics, South China Normal University, Guangzhou 510006, People's Republic of China*

[2] *Shenzhen Guohua Optoelectronics Tech. Co. Ltd., Shenzhen 518110, People's Republic of China*

[3] *Institute for Advanced Materials, South China Academy of Advanced Optoelectronics, South China Normal University, Guangzhou 510006, People's Republic of China*

(Received 2 August 2022; revised 6 December 2022; accepted 6 January 2023; published 2 February 2023)

Time-dependent dielectric breakdown (TDDB) is a crucial issue for the dielectric reliability. In this work, we present a full three-dimensional mechanistic model for calculation of the TDDB process in polycrystalline thin films. The model is based on the multiphonon trap-assisted tunneling theory and takes into account the intrinsic three-dimensional discreteness of traps at the dielectric grain boundaries. The leakage current density is calculated by solving coupled three-dimensional master equation and Poisson equation. The net phonon emission associated with each charge trapping and release event is treated as a local point heat source, which then enters the Fourier heat equation for three-dimensional temperature distribution calculation. The generated trap is determined by local temperature and electric field, which is subsequently included in the next round of calculation of electric and thermal properties. A positive feedback loop gradually leads to an increase of trap density, temperature, and leakage current density, and finally the dielectric breakdown. Our model can, to a good approximation, reproduce the experimental leakage current density-voltage characteristics and the Weibull distribution of time to breakdown at different dielectric thicknesses, stress voltages, and environmental temperatures. We find that in realistic devices, the three-dimensional trap-to-trap transport of electrons contributes a non-negligible part to the leakage current when the dielectric approaches breakdown. Our approach of three-dimensional mechanistic simulation is computationally efficient such that evolution of 10^3 traps during the TDDB process can be easily performed on a standard desktop computer.

DOI: 10.1103/PhysRevApplied.19.024008

I. INTRODUCTION

Dielectric thin films are key components of modern semiconductor devices such as transistors, capacitors, and memories. The degradation and breakdown of dielectrics significantly affect device reliability and hamper device performance and lifetime [1–5]. Unlike high-quality thermally grown silicon dioxide, deposited polycrystalline or amorphous dielectric materials (e.g., high-κ dielectrics) are more susceptible to defects, which tend to degrade over time under electrical or thermal stress (time-dependent dielectric breakdown, TDDB) [6,7]. TDDB can be characterized from a time-dependent increase of leakage current, temperature, and number of defects. Understanding the physical mechanism of TDDB through modeling and simulation are essential to rational device design, optimization, and prediction.

Research on TDDB modeling has already progressed for decades. Many phenomenological and empirical models, e.g., thermochemical model (E model) [8,9], anode hole injection model ($1/E$ model) [9,10], anode hole release model [11–13], exponential $E^{1/2}$ model [14], and etc., were proposed to explain TDDB experimental data at various electrical or thermal stress conditions. For example, the thermochemical E model provides a description of the chemical bond breakage due to bond vibration with an external-electric-field-lowered activation energy. The anode hole injection $1/E$ model is based on the idea that holes generated at the anode due to impact ionization are responsible for oxide damage. Although these models provide simple physical pictures, they are insufficient to describe the interplay of complicated and delicate physical mechanisms responsible for dielectric breakdown.

---

[*] feilongliu@m.scnu.edu.cn
[†] guofu.zhou@m.scnu.edu.cn

© 2023 American Physical Society

Percolation and leakage current filaments via multiple defects in an dielectric also play a crucial role in the TDDB process [15–17]. The generation of oxygen atomic vacancies, which can trap and release electrons, gradually forms percolative bonds for charge transport, and dielectric breakdown occurs when an overall percolation path is formed from anode to cathode. However, although percolation is an intrinsic nature of TDDB, its entire picture should, in principle, involve more physics such as the energy landscape of defects for charge trapping and transport, in addition to the geometrical effects due to spatial distribution of traps.

In recent years, more advanced mechanistic three-dimensional (3D) leakage current and TDDB models are developed [18–27]. These models typically include most or part of the following features: (1) spatial distribution of defects in the dielectric, which are often composed of atomic oxygen vacancies and behave as trap states for charge carriers; (2) energy distribution of trap states due to local amorphous atomic environments and relative energy-level alignment with respect to conduction- and valence-band edges; (3) electron transfer rates between an electrode and a trap, and between multiple traps, according to the elastic and inelastic trap-assisted tunneling (TAT) model; (4) the effect of applied electric field on the energy levels and the subsequent charge-transfer rates; (5) statistics of a sufficiently large number of electron processes or integration over energy and space to obtain the overall leakage current and percolation network; (6) coupling to phonon-generated heat and temperature distribution, and local temperature- and electric-field-dependent defect generate rate. These models have successfully reproduced the experimental data on leakage current-voltage characteristics and the Weibull statistics of device lifetimes at various materials and device parameters, and at the same time provide useful physical insight on the reliability mechanism.

Recently, our group presented a mechanistic model for calculation of gate leakage current in multilayer stacks based on multiphonon TAT theory, taking into account the intrinsic 3D discreteness of traps in the dielectric [27]. Our model can, to a good approximation, reproduce the experimental results at different dielectric thicknesses, gate voltages, temperatures, and different gate materials. We find that in realistic devices, the 3D trap-to-trap transport of electrons contributes a non-negligible part to the gate leakage current. This contribution is more pronounced at low-voltage device operations, which is useful for low-power applications. We calculate the intrinsic fluctuation of gate leakage current due to positional and energetic disorder of traps in the dielectric, and conclude that positional disorder is more relevant than energetic disorder for realistic material parameters. The calculated gate leakage current depends sensitively on temperature, trap energy, and trap density. We provide a computationally efficient 3D master equation approach that enables 3D mechanistic simulation of 10^3 traps on the order of minutes on a standard desktop computer.

The most advanced physics-based multiscale TDDB models to date have been developed by Vandelli and Padovani *et al.* [23,26]. Based on the TAT model for leakage current, the net emitted phonon energy associated with each charge trapping and release process leads to the increase of local temperature. The trap-generation (chemical bond breakage) rate is determined by the local 3D temperature and electric field around each defect. The generated defect (trap state) enters the TAT model for charge transport. A positive feedback loop with a stepwise increase of trap density, leakage current, and local temperature describes the evolution of the TDDB process and the final dielectric breakdown.

In this work, we extend our leakage current model to TDDB. Compared to the state-of-the-art TDDB models above, we make further steps forward and add the following improvements and features. (1) While existing models assume all charge carriers penetrate through the dielectric via at maximum one trap state, we take into account the process of a charge carrier transferring between two or more traps using a full 3D approach. We show that in the TDDB process, as trap density increases, the trap-to-trap transport becomes more relevant over time, especially at breakdown. (2) Instead of using kinetic Monte Carlo (KMC) simulation for trap-assisted leakage current, which relies on the statistics of a huge number of charge-carrier dynamics, we present a much more computationally efficient algorithm—the 3D master equation approach. (3) To efficiently calculate 3D electric and temperature fields, we propose a method combining short-range field around each trap and long-range field throughout the dielectric layer [28]. (4) Because of improved computational efficiency in (2) and (3), we are able to perform TDDB calculations for a system size of $10 \times 100 \times 100$ nm^3 containing 10^3 traps. (5) We also introduce the Voronoi diagram to mimic realistic polycrystalline morphology.

This paper is organized as follows. In Sec. II, we present the 3D mechanistic TDDB model for a metal-insulator-metal (M-I-M) structure. In Sec. III, we validate the model against experimental data and discuss the underlying physics during the TDDB process. In Sec. IV, we summarize the conclusions and envision possible next steps.

II. MODEL

The TDDB model presented in this work is briefly shown as a flow diagram in Fig. 1. After we input the material and device parameters, a polycrystalline morphology is generated using the Voronoi diagram. An initial trap distribution is generated randomly on the grain boundaries (GBs). The charge-transfer rates are calculated according

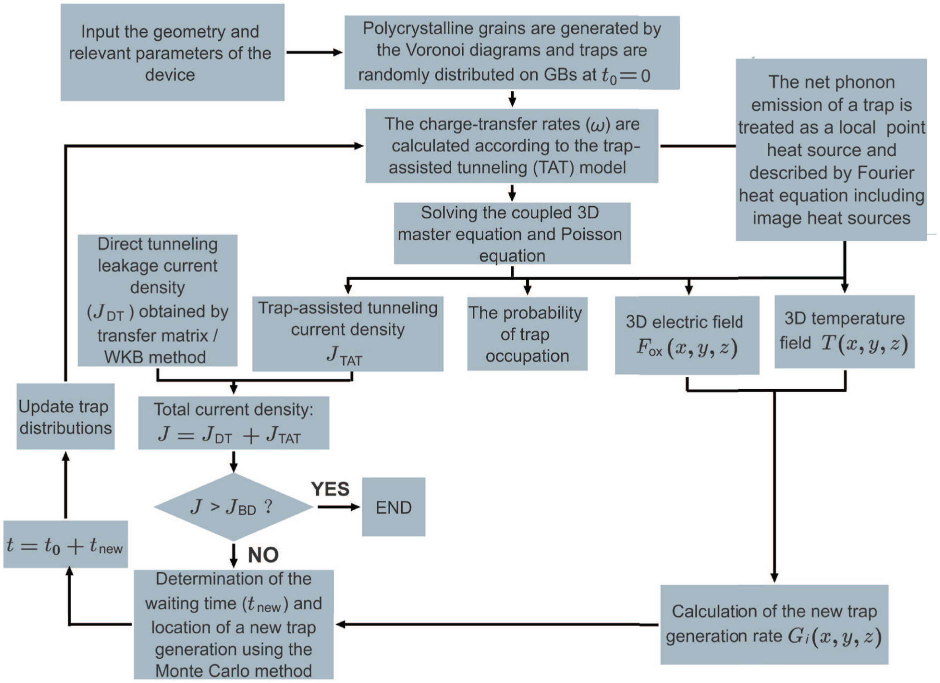

FIG. 1. Flow diagram of the TDDB model.

to the TAT model. By solving the coupled 3D master equation and Poisson equation, the trap-assisted tunneling current density, probability of trap occupation, and 3D electric field are obtained. The net phonon emission at each trap in the TAT model is treated as a local point heat source. Using the Fourier heat equation, we obtain a 3D temperature profile. The chemical bond breakage rate is dependent on local electric field and temperature. The location and interval time of a next trap is determined by a Monte Carlo process. The generated trap subsequently enters the TAT model for the next round of calculation. A positive feedback loop of gradually increasing trap number, leakage current density, local temperature, and electric field leads to dielectric breakdown. We define that the dielectric breakdown is reached as the leakage current density becomes larger than J_{BD}, which is a sufficiently large number typically set as 2×10^5 A/cm^2. The model details are described as follows.

A. Parameters

In this work, we choose a TiN-HfO$_2$-TiN sandwich structure as an example. We note that the presented model framework can, in general, be applied to other M-I-M structures. The material and device parameters are listed in Table I. A voltage V_{ox} is applied between the two electrodes. Due to the randomness of spatial and energetic distribution of traps, the calculated leakage current and time to breakdown fluctuate among different samples. We thus take sufficiently large number (e.g., 50) of different disorder configurations in the calculation.

B. Polycrystalline morphology generation

The polycrystalline grains are generated by the Voronoi topology, which is the standard technique for simulation

TABLE I. List of parameters.

Parameter	Value
Chemical bond breakage activation energy E_A	4.4 eV [23]
HfO$_2$ conduction-band minimum E_c	2.7 eV [29]
HfO$_2$ valence-band maximum E_v	−3.1 eV [30]
Effective vibration frequency of the O—Hf bond G_0	7×10^{13} Hz [23]
HfO$_2$ electron tunneling effective mass m^*_{ox}	$0.2m_e$[a] [29,31,32]
TiN electron effective mass m^*_{metal}	$2.2m_e$ [33]
Phonon energy $\hbar\omega_0$	0.085 eV [20]
Huang-Rhys factor S	25 [24,27]
Polycrystalline grain density N_G	10^{16} m^{-2} [34]
Prestress defect density in dielectric N_{T0}	8×10^{24} m^{-3} [23]
HfO$_2$ dielectric constant ε_r	25 [23]
TiN electrode work function $E_{F,L}$ (reference energy)	0 eV
Material electrical polarization factor p_0	5.2 eÅ [23,35,36]
Trap energy (mean value) E_T	0.5 eV [23]
Trap energy (deviation) σ	0.5 eV [23]
HfO$_2$ thermal conductivity k_T	0.5 W/(m · K) [37]
Minimum distance between traps a	0.36 nm [38]
Hopping attempt frequency ν_0	10^{13} Hz [20]
Distance between two electrodes L_x	$5 - 8$ nm
Lateral dimensions of the system L_y, L_z	$20 - 100$ nm

[a] m_e is the free electron mass.

of the realistic growth process of polycrystalline thin films [39]. For an ultrathin dielectric layer (e.g., ≤ 10 nm), because its thickness is much smaller than its lateral dimensions, we assume the GBs are normal to the substrate for simplicity. We use periodic boundary condition in y and z directions for the Voronoi topology generation.

Due to local atomic environments, chemical bonds tend to break much easier at GBs than inside single-crystal grains [40,41]. For example, by using first-principles calculation, McKenna *et al.* showed that the ratio of traps generated at the GBs f_{GB} to traps generated inside grains f_{bulk} is determined by a segregation energy E_s and temperature T as $f_{\text{GB}}/f_{\text{bulk}} = \exp(-E_s/k_BT)$ [38]. Their calculation results show that $f_{\text{GB}}/f_{\text{bulk}}$ is around 87 for m-HfO$_2$ at $T = 1300$ K, and the number is expected to increase by orders of magnitude at room temperature. Therefore, we consider only traps in GB planes in this work for simplicity. The minimum distance between traps at the GBs is set to be 0.36 nm, which is limited by the chemical bond length and is also obtained from atomic first-principles calculations [38]. The initial trap concentration and energetic distribution parameters are determined by calculating the temperature- and voltage-dependent leakage current density and comparing with experimental results before the TDDB stress. Due to the complexity of the amorphous nature at the GBs, the trap (primarily oxygen vacancies) energy is widely distributed in the band gap. Here we assume that the energy of each trap is taken randomly from a uniform distribution in the range of $E_T \pm \sigma$ [23]. In addition, the trap energy is modified by the local electrostatic potential as described in the following sections.

C. Charge-transfer rates

The charge-transfer rates are calculated by the effective-mass-based semiclassical TAT approach [20,21,27,42]. The following processes are considered in our model, as shown in Fig. 2. (1) We consider both elastic and inelastic charge-transfer processes between a metal electrode and a trap in the dielectric. For the elastic process, the energy of an injecting electron in the metal is equal to the trap energy, and no phonon is involved during the process. For the inelastic process, the energy of the incoming electron at the electrode is different from the energy of a trap, and the energy difference is associated with absorbing or emitting multiple phonons (lattice vibration). The inelastic (elastic) process rates are shown in Eqs. (1) and (2) [Eqs. (3) and (4)]. (2) Charge-transfer between two traps. This process is considered as an incoherent hopping event and is described by the Miller-Abrahams formula in Eq. (6). We also allow for the direct tunneling process through trapzoidal or triangular barriers using the transfer matrix and WKB method [Eqs. (10) and (11)] [27].

$$\omega^{\text{inela}}_{L/R\to\text{trap},i} = c_{0,i}\left[\sum_{m<0}^{-\infty} g_{L/R}(E_{m,i}) f\,(E_{m,i}, E_{F,L/R}, T_i)\bar{T}(E_{m,i}, x_{L/R}, x_i)L_m(T_i)\exp\left(\frac{m\hbar\omega_0}{k_BT_i}\right)\right.$$
$$\left. + \sum_{m>0}^{+\infty} g_{L/R}(E_{m,i}) f\,(E_{m,i}, E_{F,L/R}, T_i)\bar{T}(E_{m,i}, x_{L/R}, x_i)L_m(T_i)\right], \tag{1}$$

$$\omega^{\text{inela}}_{\text{trap}\to L/R,i} = c_{0,i}\left[\sum_{m<0}^{-\infty} g_{L/R}(E_{m,i})\big(1 - f\,(E_{m,i}, E_{F,L/R}, T_i)\big)\bar{T}(E_{m,i}, x_i, x_{L/R})L_m(T_i)\right.$$
$$\left. + \sum_{m>0}^{+\infty} g_{L/R}(E_{m,i})\big(1 - f\,(E_{m,i}, E_{F,L/R}, T_i)\big)\bar{T}(E_{m,i}, x_i, x_{L/R})L_m(T_i)\exp\left(-\frac{m\hbar\omega_0}{k_BT_i}\right)\right], \tag{2}$$

$$\omega^{\text{ela}}_{L/R\to trap,i} = \left(\frac{m^*_{\text{metal}}}{m^*_{\text{ox}}}\right)^{5/2} \frac{8(E_{T,i} - E_{F,L/R})^{3/2}}{3\hbar\sqrt{E_{D,i}}} f\,(E_{T,i}, E_{F,L/R}, T_i)\bar{T}(E_{T,i}, x_{L/R}, x_i), \tag{3}$$

$$\omega^{\text{ela}}_{\text{trap}\to L/R,i} = \left(\frac{m^*_{\text{metal}}}{m^*_{\text{ox}}}\right)^{5/2} \frac{8(E_{T,i} - E_{F,L/R})^{3/2}}{3\hbar\sqrt{E_{D,i}}}\big(1 - f\,(E_{T,i}, E_{F,L/R}, T_i)\big)\bar{T}(E_{T,i}, x_i, x_{L/R}). \tag{4}$$

The prefactor $c_{0,i}$ is given by $c_{0,i} = (4\pi)^2R_{t,i}^3/E_ge^2\hbar F_i^2/2m^*_{\text{ox}}$, with $R_{t,i} = \hbar/\sqrt{2m^*_{\text{ox}}E_{D,i}}$ the localization radius of the trapped electron in trap i [43]. $E_g = E_c - E_v$ is the band gap. e is the elementary charge. $\hbar$ is the reduced Planck constant. F_i is the local electric field at trap i. $E_{D,i} = E_c - E_i$ is the trap energy with respect to the conduction-band

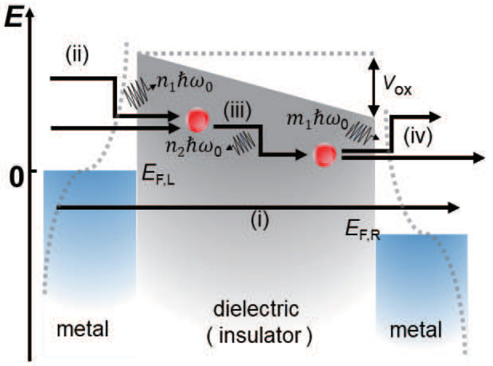

FIG. 2. Energy level diagram and charge transfer processes of a metal-insulator-metal (*M-I-M*) structure with an applied voltage V_{ox}. The charge transfer mechanisms considered in the model are: (i) direct tunneling; (ii) elastic/inelastic tunneling of an electron from the cathode to a trap; (iii) trap-to-trap tunneling; and (iv) elastic/inelastic tunneling from a trap to the anode.

edge. $x_L = 0$ and $x_R = L_x$ are the locations of the two electrodes. The location of trap i is (x_i, y_i, z_i). $f(E_i, E_F, T_i) = [\exp(E_i - E_F/k_B T_i) + 1]^{-1}$ is the Fermi-Dirac distribution. $E_{F,L/R}$ is the Fermi level of the left or right electrode. $E_{F,R} = E_{F,L} - eV_{\mathrm{ox}}$. T_i is the local temperature at trap i. $E_{m,i} = E_{T,i} + m\hbar\omega_0$ is the trap energy plus $(m > 0)$ or minus $(m < 0)$ the phonon energy associated with the transition. m is the number of phonons involved in the charge transfer. $\bar{T}$ is the transmission coefficient calculated using the WKB method [27]. L_m is associated with the multiphonon transition probability and describes the electron-phonon coupling strength:

$$L_m = \left(\frac{f_B + 1}{f_B}\right)^{|m|/2} \exp\left[-S\left(2f_B + 1\right)\right] I_{|m|}(z), \qquad (5)$$

where $z = 2S\sqrt{f_B\left(f_B + 1\right)}$, $I_{|m|}(z)$ is the modified Bessel function of order $|m|$, and $f_B(T_i) = [\exp(\hbar\omega_0/k_B T_i) - 1]^{-1}$ is the Bose-Einstein distribution. The density of states (g) of electrodes is assumed to be parabolic, $g_{L/R}(E) = 1/2\pi^2\left(2m^*_{\mathrm{metal}}/\hbar^2\right)^{3/2}\sqrt{E - E_{F,L/R}}\,\Theta(E - E_{F,L/R})$, where Θ is the Heaviside step function.

The charge-transfer rate between two traps is treated as an incoherent hopping process and obtained by the Miller-Abrahams formula [44]

$$\omega_{i\to j} = \nu_0 \exp\left(-\frac{r_{ij}}{R_{t,i}}\right) \exp\left(-\frac{r_{ij}}{R_{t,j}}\right) \times \begin{cases} e^{-2(E_j - E_i)/(k_B(T_i + T_j))}, & E_j - E_i > 0, \\ 1, & E_j - E_i \leqslant 0, \end{cases} \qquad (6)$$

where $r_{ij} = \sqrt{(x_i - x_j)^2 + (y_i - y_j)^2 + (z_i - z_j)^2}$. Periodic boundary condition is assumed in y and z directions.

When two traps are spatially close to each other, the trapped electron wave function tends to delocalize. This effect is modeled as a decrease of the phonon energy $\hbar\omega_0$ with intertrap distance [23,45,46]:

$$\hbar\omega_{0,ij} = \hbar\omega_0\left[1 - \exp\left(-\frac{r_{ij}}{\max(R_{t,i}, R_{t,j})}\right)\right]. \qquad (7)$$

D. Calculation of leakage current density

The leakage current density in our model consists of two parts, the TAT current density J_{TAT}, and the direct tunneling current density J_{DT}. The total leakage current density is then $J = J_{\mathrm{DT}} + J_{\mathrm{TAT}}$.

J_{TAT} is calculated using the 3D master equation approach. Instead of following the dynamics of every electron for statistics in KMC, the 3D master equation calculates the evolution of electron occupation probability of each trap p_i. Compared to KMC, the 3D master equation approach significantly improves numerical efficiency while maintaining the accuracy of physics [27]. At steady state, the charge capture and release rates associated with each trap are balanced, described as

$$\sum_j [\omega_{i\to j} p_i(1 - p_j) - \omega_{j\to i} p_j(1 - p_i)] = -\frac{dp_i}{dt} = 0, \qquad (8)$$

where the term $1 - p_i$ excludes multiple electrons occupying a single trap at the same time. The 3D master equation is coupled to the electrostatic Poisson equation and solved for p_i at all the traps using Newton's iteration method. J_{TAT} is then obtained as a sum of all charge-transfer processes along the direction of the applied electric field:

$$J_{\mathrm{TAT}} = \frac{e}{L_x L_y L_z} \sum_{i,j} \omega_{i\to j} p_i (1 - p_j)(x_j - x_i). \qquad (9)$$

The direct tunneling current density J_{DT} is calculated through the Tsu-Esaki equation [47].

$$J_{\mathrm{DT}} = \frac{m^*_{\mathrm{metal}} e k_B T}{2\pi^2\hbar^3} \int_{E_{F,L}}^{+\infty} \bar{T}(E) N(E)\, dE, \qquad (10)$$

$$N(E) = \ln\left[\frac{1 + \exp\left(\frac{E_{F,L} - E}{k_B T}\right)}{1 + \exp\left(\frac{E_{F,R} - E}{k_B T}\right)}\right], \qquad (11)$$

where $N(E)$ is the supply function. J_{DT} is typically much smaller than J_{TAT}, but is not negligible at high voltage stresses and small dielectric thicknesses [27].

E. Calculation of 3D temperature

Assuming that the thermal conductivity of the dielectric is homogeneous and the heat flow is sufficiently fast, the

Fourier heat diffusion equation [Eq. (12)] can be reduced to its steady-state form [Eq. (13)]:

$$\nabla(k_T\nabla T) + P = \rho C_p \frac{\partial T}{\partial t}, \tag{12}$$

$$P = -k_T \nabla^2 T, \tag{13}$$

where k_T is thermal conductivity, P is the heat generation rate per unit volume, ρ is the material density, and C_p is the specific heat capacity. A justification of the steady-state heat transport is discussed in Sec. S1 within the Supplemental Material [48]. The heat power generation from individual traps can be described by a sum of Dirac δ functions:

$$P(\vec{r}_i) = \sum_i P_i \delta^3(\vec{r} - \vec{r}_i). \tag{14}$$

By using the mathematical formula $\nabla^2 1/r = -4\pi\delta^3(r)$, Eqs. (13) and (14) can be converted from differential equations to algebraic equations. Due to the fact that metallic electrodes typically have a larger thermal conductivity than the dielectric, we further assume that the two electrodes are ideal heat sinks and their temperature is always equal to the ambient temperature. Similar to the electrostatics where metallic electrodes are considered as ideal electrical conductors and behave as mirrors for point charges outside, here we employ a similar "mirror heat image" method to calculate the 3D temperature distribution in the presence of two isothermal electrodes in parallel [28]:

$$T(x,y,z) = \frac{1}{4\pi k_T}\sum_i \left[\frac{P_i}{\sqrt{(x-x_i)^2+(y-y_i)^2+(z-z_i)^2}} - \sum_{n=-n_{\mathrm{img}}}^{n_{\mathrm{img}}} \frac{P_i}{\sqrt{(x+x_i+2nL_x)^2+(y-y_i)^2+(z-z_i)^2}} \right.$$
$$\left. + \sum_{n=-n_{\mathrm{img}},n\neq 0}^{n_{\mathrm{img}}} \frac{P_i}{\sqrt{(x-x_i+2nL_x)^2+(y-y_i)^2+(z-z_i)^2}}\right] + T_{\mathrm{env}}, \tag{15}$$

where T_{env} is the ambient environmental temperature and n_{img} is the number of heat-mirror images. We take a large enough number $n_{\mathrm{img}} = 100$ so that further increase of n_{img} does not affect the results. We note that Eq. (15) is only valid for a uniform thermal conductivity. However, due to lattice mismatch, the thermal conductivity at grain boundaries is in general smaller than that inside grains and a "hot spot" could be generated due to thermal insulation of grain boundaries. We further discuss this topic in Sec. S2 within the Supplemental Material [48].

The heat-generation power is linked to the net number of emitted phonons associated with each trap during the charge-transfer processes:

$$P_i^{L/R\to i} = \hbar\omega_0(1-p_i)\sum_m \omega_{L/R\to i,m}^{\mathrm{inela}} m, \tag{16}$$

$$P_i^{i\to L/R} = \hbar\omega_0 p_i \sum_m \omega_{i\to L/R,m}^{\mathrm{inela}} m, \tag{17}$$

$$P_i^{i\to j} = \begin{cases} \omega_{i\to j} p_i(1-p_j)(E_i - E_j), & E_j - E_i > 0, \\ 0, & E_j - E_i \leqslant 0, \end{cases} \tag{18}$$

$$P_j^{i\to j} = \begin{cases} 0, & E_j - E_i > 0, \\ \omega_{i\to j} p_i(1-p_j)(E_i - E_j), & E_j - E_i \leqslant 0. \end{cases} \tag{19}$$

Here $P_i^{L/R\to i}$ ($P_i^{i\to L/R}$) is the power-generation rate at trap i during the process of an electron transfer from an electrode (the trap) to the trap (an electrode). $\omega_{L/R\to i,m}^{\mathrm{inela}}$ ($\omega_{i\to L/R,m}^{\mathrm{inela}}$) is the inelastic charge-transfer rate from an electrode (trap i) to trap i (an electrode) associated with m phonons. $m > 0$ ($m < 0$) denotes phonon emission (absorption). $P_i^{i\to j}$ ($P_j^{i\to j}$) is the power-generation rate at trap i (j) during the process of an electron transfer from trap i to trap j.

F. Calculation of 3D electric field

In the vicinity of each trap, the 3D feature of local electric field due to the trapped charge is crucial for accurately calculating the next trap-generation rate. To efficiently calculate the 3D electric field due to both the applied voltage and the trapped charge, the 3D Poisson equation is simplified as a combination of long-range and short-range contributions [28]. Far from each trap, the long-range electric field $F_{\mathrm{LR}}(x_i)$ is obtained from the one-dimensional (1D) discrete Poission equation along x direction. Within each discretization step $\Delta x = x_{i+1} - x_i$, the trapped charge density ρ_{x_i} is layer averaged over the y-z plane. Within a cutoff radius R_C around each trap, the short-range electric field at a possible trap-generation site i due to charge-carrier occupation at an existing trap j, $F_{\mathrm{SR}}(i,j)$, is obtained from the 3D Poisson equation including the mirror-image charges generated by two parallel electrodes:

$$F_{\mathrm{SR}}(i,j) = \frac{ep_j}{4\pi\varepsilon_0\varepsilon_r}\Bigg[\frac{1}{(x_j - x_i)^2 + (y_j - y_i)^2 + (z_j - z_i)^2} - \sum_{n=-n_{\mathrm{img}}}^{n_{\mathrm{img}}} \frac{1}{(x_j + x_i + 2nL_x)^2 + (y_j - y_i)^2 + (z_j - z_i)^2} + \sum_{n=-n_{\mathrm{img}},n\neq 0}^{n_{\mathrm{img}}} \frac{1}{(x_j - x_i + 2nL_x)^2 + (y_j - y_i)^2 + (z_j - z_i)^2}\Bigg], \tag{20}$$

$$F_{\mathrm{SR}}(i,j)_x = F_{\mathrm{SR}}(i,j)\frac{x_i - x_j}{\sqrt{(x_j - x_i)^2 + (y_j - y_i)^2 + (z_j - z_i)^2}}, \tag{21}$$

$$F_{\mathrm{SR}}(i,j)_y = F_{\mathrm{SR}}(i,j)\frac{y_i - y_j}{\sqrt{(x_j - x_i)^2 + (y_j - y_i)^2 + (z_j - z_i)^2}}, \tag{22}$$

$$F_{\mathrm{SR}}(i,j)_z = F_{\mathrm{SR}}(i,j)\frac{z_i - z_j}{\sqrt{(x_j - x_i)^2 + (y_j - y_i)^2 + (z_j - z_i)^2}}, \tag{23}$$

with ε_0 the vacuum permittivity. To avoid double counting of both long-range and short-range fields within the cutoff radius, a correction term to the electric field at a possible trap-generation site i due to disk charge density of layer x_j, $F_{\mathrm{disk}}(i,x_j)_x$, needs to be included:

$$F_{\mathrm{disk}}(i,x_j)_x = \frac{\rho_{x_j}}{2\varepsilon_0\varepsilon_r}\Bigg[\mathrm{sgn}(x_j - x_i)\left(1 - \frac{|x_j - x_i|}{R_C}\right) - \sum_{n=-n_{\mathrm{disk}}}^{n_{\mathrm{disk}}} \mathrm{sgn}(x_j + x_i + 2nL_x)\left(1 - \frac{|x_j + x_i + 2nL_x|}{\sqrt{R^2_{x_j - x_i} + (x_j + x_i + 2nL_x)^2}}\right) + \sum_{n=-n_{\mathrm{disk}},n\neq 0}^{n_{\mathrm{disk}}} \mathrm{sgn}(x_j - x_i + 2nL_x)\left(1 - \frac{|x_j - x_i + 2nL_x|}{\sqrt{R^2_{x_j - x_i} + (x_j - x_i + 2nL_x)^2}}\right)\Bigg], \tag{24}$$

where $R^2_{x_j - x_i} = R_C^2 - (x_j - x_i)^2$. In the limit of $R_C \to 0$, the electric field calculation reduces to purely 1D. In the limit of $R_C \to \infty$, the electric field calculation is fully 3D, but the calculation is very slow. In this work, to maintain both physical accuracy and numerical efficiency, we choose $R_C = 3.6$ nm and ensure that further increasing R_C does not affect the calculation results.

G. Calculation of next trap generation

After the 3D temperature and electric field profiles are obtained, the position-dependent next trap-generation rate $G_F(x,y,z)$ is determined as

$$G_F(x,y,z) = G_0 \exp\left(-\frac{E_A - b|F_{\mathrm{ox}}(x,y,z)|}{k_B T(x,y,z)}\right), \tag{25}$$

where $b = p_0[(2 + \varepsilon_r)/3]$ is the bond polarization factor. The location of a generated trap is obtained from the standard Monte Carlo approach. The time interval of trap generation is calculated from the standard exponential waiting time distribution. The generated trap, together with all existing traps, subsequently enter the next round of calculation for charge transfer, leakage current density, temperature, and electric field.

In this work, the microscopic picture of trap generation is assumed to be oxygen vacancy formation directly due to the electric field. However, we note that recent work from first-principles studies shows that the dipole moment of defects and bonds is generally not strong enough to directly induce a significant barrier lowering for dissociation by the electric field. Instead, electron injection into self-trapped states in the a-HfO$_2$ [so-called (bi)polarons] leads to a significant reduction of the barrier to form Frenkel-pair defects [49,50]. In this situation, the physical meaning of G_0 would then be the rate of the double electron capture process occurring at precursor sites, E_A would then become the zero-field bond-breaking energy associated with a precursor site with two trapped electrons, and b would be the effective dipole moment at the saddle point (relative to the initial-state dipole) in the zero-field reaction pathway [50].

III. RESULTS AND DISCUSSION

Figure 3 shows the measured and simulated prestress leakage current density-voltage characteristics of a 5-nm-thick TiN-HfO$_2$-TiN device at different temperatures. The experimental data are from Ref. [23]. By comparing simulation results with experiment, the prestress trap density and trap energy (mean value and standard deviation) are extracted (Table I). The good agreement between simulation and experiment at various temperatures and voltages indicates that the model presented can well capture the trap-assisted charge transport in the dielectric.

In Fig. 4, we perform TDDB simulations of a 5-nm-thick TiN-HfO$_2$-TiN device at $T_{\text{env}} = 398$ K with two constant voltage stresses $V_{\text{ox}} = 3.1$ and 3.2 V. The breakdown time among different samples follows the Weibull distribution, with the cumulative distribution function F given by

$$F = 1 - \exp\left[-\left(\frac{t_{\text{BD}}}{\lambda}\right)^k\right], \tag{26}$$

where $\lambda > 0$ is the scale parameter and $k > 0$ is the shape parameter. By plotting $\ln(-\ln(1-F))$ versus t_{BD}, a straight line with a slope k can be obtained. The simulated t_{BD} distribution agrees well with experimental results, obtained from Ref. [23]. By varying the applied stress voltage V_{ox}, the value of material electrical polarization factor p_0 is extracted. The obtained slope $k \approx 1.5 > 1$, meaning that the failure rate increases with time. This indicates that the dielectric TDDB is an "aging" process.

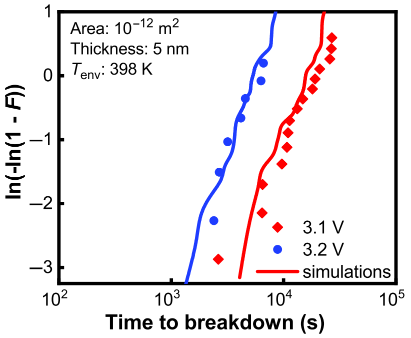

FIG. 4. Calculated (curves) and experimental (symbols) TDDB Weibull distributions of a 5-nm-thick TiN-HfO$_2$-TiN device at two different voltage stress conditions.

Figure 5 shows the measured [23] and simulated Weibull distributions of breakdown time of a 7-nm-thick TiN-HfO$_2$-TiN device at different temperatures. Good agreement is obtained and the chemical bond breakage activation energy E_A is extracted. The Weibull slope in this figure is approximately 2–3, larger than that in Fig. 4. This result agrees with previous research and is known to be a percolation effect [15,16].

Figures 4 and 5 correspond to different device areas. It is well known that the time to breakdown depends sensitively on the area. For two samples with areas A_1 and A_2, the ratio of t_{BD2} to t_{BD1} is given by [16]

$$\frac{t_{\text{BD2}}}{t_{\text{BD1}}} = \left(\frac{A_2}{A_1}\right)^{-1/k}. \tag{27}$$

This scaling rule, however, is only obtained from statistical effects. If the dimension of simulated dielectric sample is too small, one would expect that the temperature and electric field increase during TDDB is not negligible at the boundaries of the simulation box. Therefore, a crosstalk between neighboring samples would occur. To avoid this effect, we choose sufficiently large simulation boxes with lateral dimensions $L_x \times L_y > 400$ nm^2. We validate our model by further increasing the device area and comparing the scaling of breakdown time, as shown in Fig. 6. The

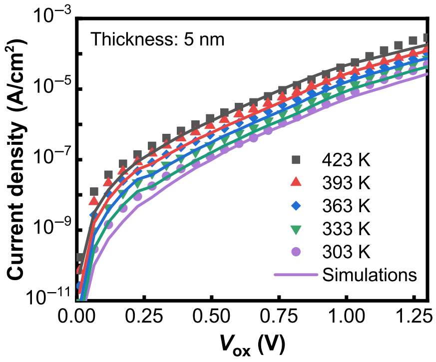

FIG. 3. Calculated (curves) and experimental (symbols) prestress leakage current density-voltage characteristics of a 5-nm-thick TiN-HfO$_2$-TiN device at various environmental temperatures.

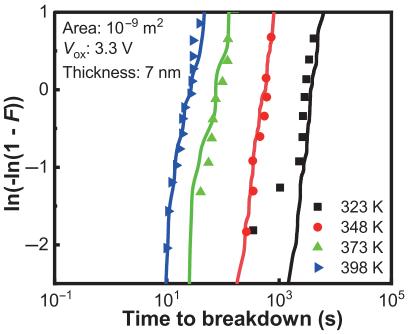

FIG. 5. Calculated (curves) and experimental (symbols) TDDB Weibull distributions of a 7-nm-thick TiN-HfO$_2$-TiN device subjected to a voltage stress at different environmental temperatures.

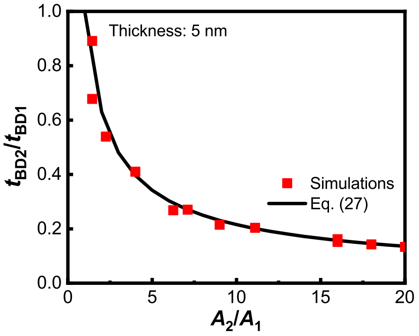

FIG. 6. Scaling of breakdown time t_{BD} to device area A, calculated from Eq. (27) (curve) and full 3D simulation (symbols) of a 5-nm-thick TiN-HfO$_2$-TiN device at $T_{\mathrm{env}} = 398$ K and $V_{\mathrm{ox}} = 3.2$ V.

simulation results agree well with Eq. (27), showing that the crosstalk effect is insignificant in our simulation. After the area scaling is validated, simulation of an arbitrarily large device (e.g., 10^{-12} or 10^{-9} m^2) can be simplified as a combination of a smaller device simulation and Eq. (27).

The effect of trap recombination, phonon energy, bond polarizability, and grain properties on TDDB are discussed in Secs. S3–S6 within the Supplemental Material [48]. Trap recombination could partially "heal" the device and decay the TDDB process. A smaller phonon energy can enhance electron-phonon coupling, and thus reduce the time to breakdown. The bond polarizability can significantly affect the voltage dependence of TDDB. Because in our model TDDB occurs only due to traps along grain boundaries, increasing the grain density would speed up the TDDB process.

To gain further insight into the progressive degradation of the dielectric, we analyze the evolution of maximum temperature, number of traps, current density, and the fraction of trap-to-trap contribution to the total leakage current in Fig. 7. We observe that the gradual increase of current density and trap number occurs earlier than an abrupt increase of the maximum temperature. Once the onset of temperature increase appears, the TDDB process immediately becomes accelerated and the dielectric quickly breaks down. For this example a 5-nm-thick device at 3.2 V, the ratio of trap-to-trap current to the total current density $J_{\mathrm{trap-trap}}/J$ is very small before TDDB occurs, which is consistent with our previous studies [27]. Near breakdown, $J_{\text{trap-trap}}/J$ increases sharply and can reach 10^{-2}–10^{-1}.

In Fig. 8, we further analyze the evolution of $J_{\text{trap-trap}}/J$ for a thicker (8 nm) device. It is observed that the trap-to-trap transport during TDDB is more important. Especially near breakdown, $J_{\text{trap-trap}}/J$ could reach as high as 40% of the total leakage current. This result shows that the full 3D modeling of the charge transport including trap-to-trap contribution, as described in this paper, is crucial to accurately describe the physics of the TDDB process.

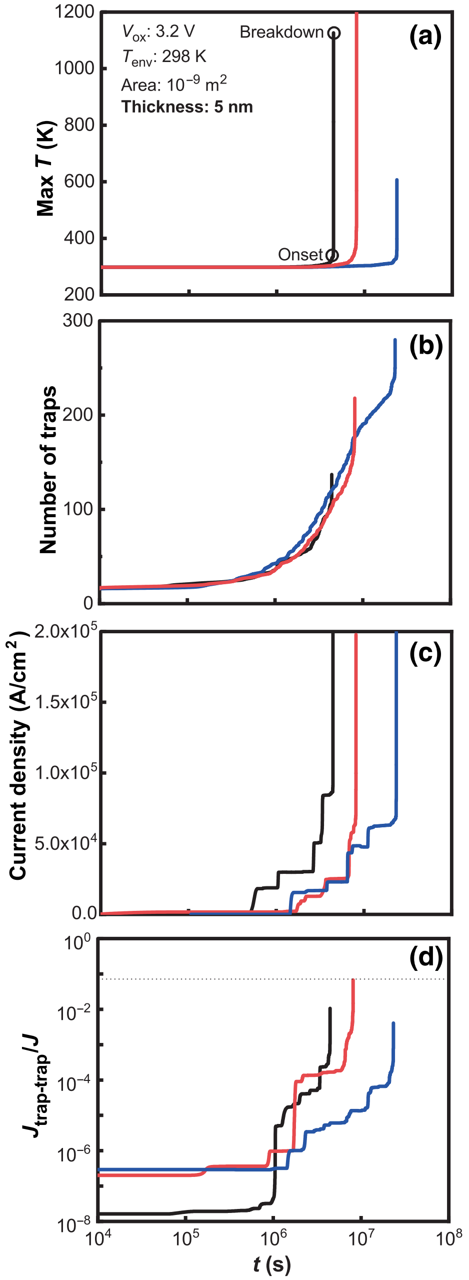

FIG. 7. Evolution of (a) maximum temperature, (b) number of traps, (c) current density, and (d) fraction of trap-to-trap contribution to the total leakage current of a 5-nm-thick TiN-HfO$_2$-TiN device. Results shown are for three different samples.

Figure 9 shows the spatial distribution of the GBs and the evolution of trap sites. Before stress ($t = 0$), an initial density of traps is determined by the prestress current density in Fig. 3 and randomly located at the GB interfaces. As TDDB progresses, the trap number grows and its spatial distribution varies among different cases. At a large voltage and a high temperature [Figs. 9(a)–9(c)], the traps are generated more randomly before t_{onset} and more correlated in clusters after t_{onset}. At a low voltage and a

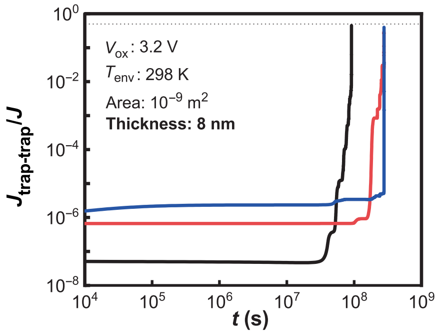

FIG. 8. Evolution of fraction of trap-to-trap contribution to the total leakage current of 8-nm-thick TiN-HfO$_2$-TiN device. Results shown are for three different samples.

high temperature, the traps are always generated in clusters [Figs. 9(d)–9(f)]. At a large voltage and a low temperature [Figs. 9(g)–9(i)], the results are similar to the large voltage and high temperature case. These results can be understood as follows. Before t_{onset}, because the system is close to an isothermal state, the next trap generation is mainly determined by the local electric field [Eq. (25)]. At a large voltage, the externally applied electric field dominates over the local electric field around each trap due to trapped charge carriers, a near-uniform trap-generation probability is maintained throughout the entire system. At a low voltage, the local electric field dominates and the next trap-generation probability is higher around existing traps, resulting in spatial correlation of trap generation. After t_{onset}, the maximum temperature in the system dramatically increases around high-power traps, therefore the next trap-generation rate is now determined by the temperature effect. The traps always form clusters. The electric field effect now becomes less relevant.

Figure 10 shows the calculated temperature profile of three representative GB surfaces at the onset (a) and breakdown (b) time. At the onset of TDDB, the overall temperature of the entire device is close to the environmental temperature and the spatial variation of temperature distribution is small. When reaching breakdown, the temperature increases dramatically around a local trap cluster due to the large electrical current transferred into heat. Even at breakdown, the temperature of the left GB plane does not differ much from the environment. The breakdown is mainly due to the trap cluster at the corner formed between the middle and right GB planes.

Figure 11 shows the calculated corresponding vectorized electric field profile for the case of Fig. 10. For the left GB plane, the external applied voltage is dominant.

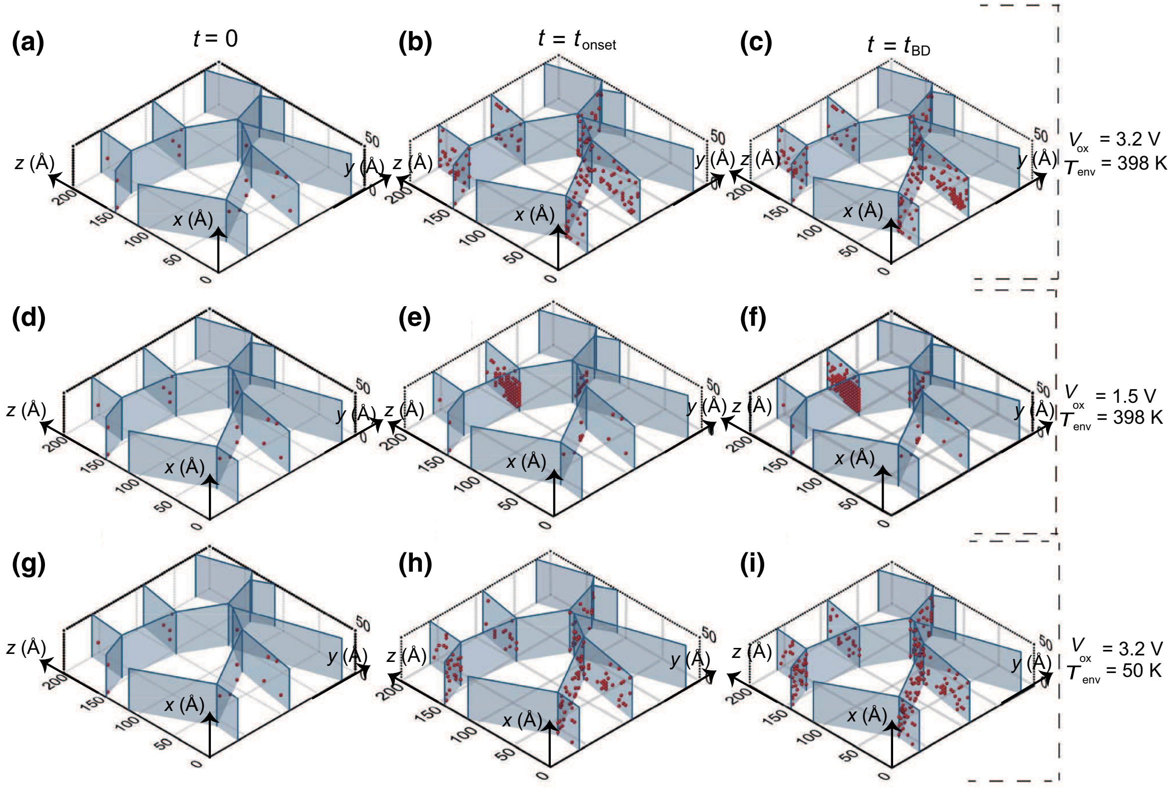

FIG. 9. Evolution of 3D spatial distributions of traps (red dots) at GBs in a 5-nm-thick TiN-HfO$_2$-TiN *M-I-M* device from prestress [(a),(d),(g)], onset [(b),(e),(h)], to breakdown [(c),(f),(i)]. (a)–(c) $T_{\text{env}} = 398$ K and $V_{\text{ox}} = 3.2$ V; (d)–(f) $T_{\text{env}} = 398$ K and $V_{\text{ox}} = 1.5$ V; (g)–(i) $T_{\text{env}} = 50$ K and $V_{\text{ox}} = 3.2$ V.

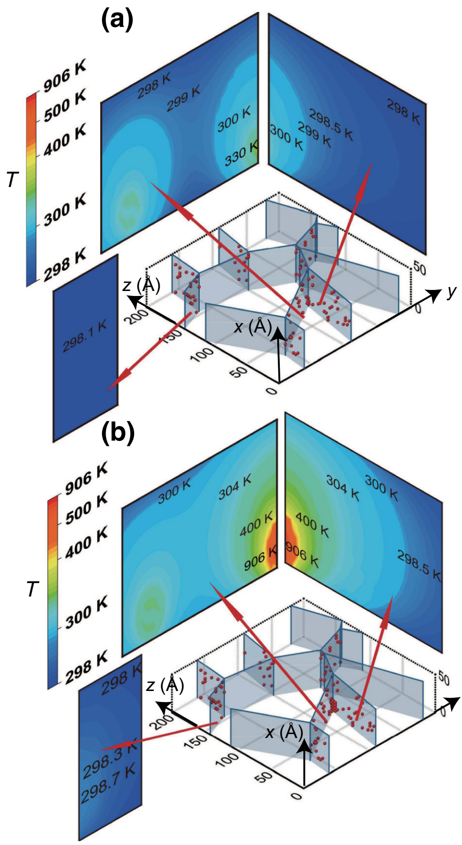

FIG. 10. Calculated temperature profiles of three representative GB interfaces at (a) onset time and (b) time to breakdown of a 5-nm-thick TiN-HfO$_2$-TiN device under stress of $V_{\text{ox}} = 3.2$ V and $T_{\text{env}} = 298$ K.

The electric field is uniform and along x direction. For the two other GB planes in which TDDB occurs, a significant amount of charge carriers are trapped in the cluster and the electric field profile is greatly modified by these trapped charges. Figures 10 and 11 show that calculation of temperature and electric field in 3D are crucial in modeling TDDB physics.

A powerful aspect of our model is to identify the leakage current associated with each trap. We can address here a worthwhile question of whether the increased current during TDDB is due to the increased defect concentration or due to the enhanced trap-trap hopping rate itself. In Fig. 12, we study the contribution to the leakage current due to each part of the traps during the TDDB process. In the example shown, the TDDB simulation starts with 50 traps. As the trap number and leakage current increases with time, we can trace the leakage current due to any given trap or trap clusters. The results shown are the current contribution due to the first 50, 100, 150, and 200 traps, and the fractions to the total leakage current due to traps 1-50, 51-100, 101-150, and 151-200. When a hopping event is between two traps, we assign its contribution to the next trap for

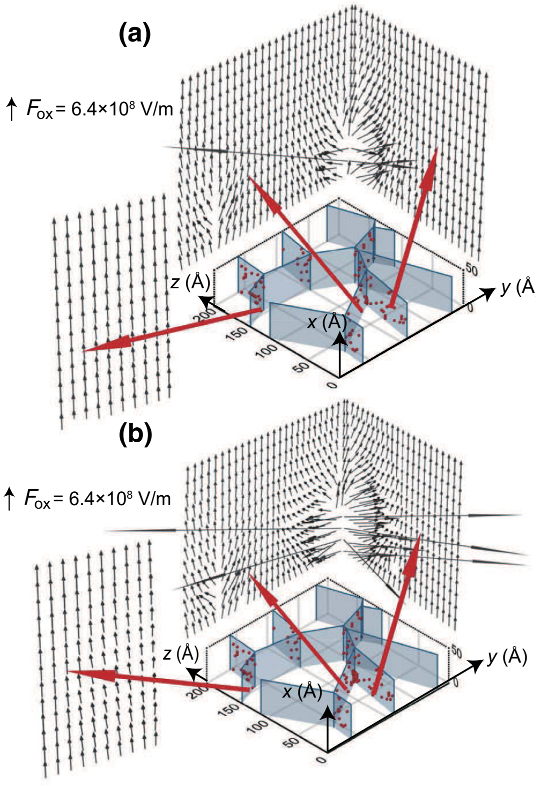

FIG. 11. Calculated electric field profiles of three representative GB interfaces at (a) onset time and (b) time to breakdown of a 5-nm-thick TiN-HfO$_2$-TiN device under stress of $V_{\text{ox}} = 3.2$ V and $T_{\text{env}} = 298$ K.

simplicity. The results show that for earlier traps, the associated leakage current is almost unchanged with time. It is probably because the old traps are separated far from each other. For latter traps closer to breakdown, their associated leakage current significantly increases with time. It is likely because that these traps are in clusters at a local hot spot. Another observation from this result is that leakage current is mainly caused by a few "favored" traps, rather than all traps, especially in the early stage of TDDB. A generated trap is likely to be very high in energy so that it can hardly accommodate any electron. In summary, at an early stage of TDDB, the increased current is mainly due to the increased defect concentration; at a later stage closer to TDDB, the increased current is due to both the increased defect concentration and the increased current due to trap-trap hopping itself.

Another powerfulness of our model is to elaborate on the significance of delicate and complicated interplay between elastic and inelastic processes. In Fig. 13, two cases are compared: (a) both elastic and inelastic processes are included; (b) the elastic processes are turned off and the TAT process contains only the inelastic processes. The current density, number of traps, maximum temperature, and fraction of trap-to-trap current in the TDDB process are

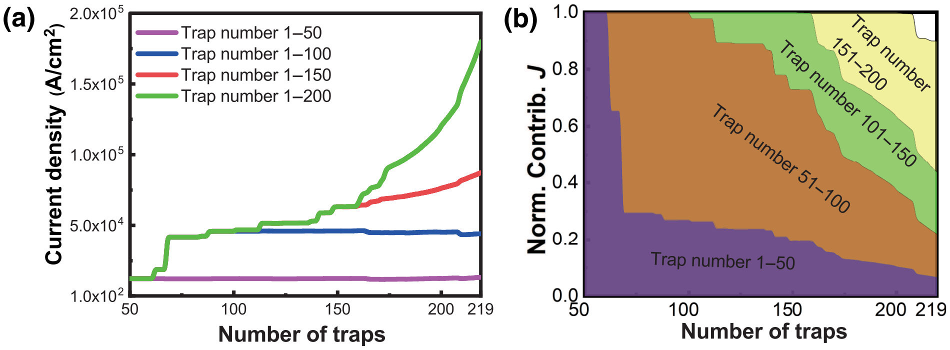

FIG. 12. Progress of contribution to leakage currents during a TDDB process starting from 50 traps. (a) Leakage currents from the first 50, 100, 150, and 200 traps as a function of the total trap number. (b) Normalized contribution to the total leakage current from traps 1-50, 51-100, 101-150, and 151-200.

compared for cases (a) and (b). First we observe that the current due to elastic processes are orders of magnitude higher than that due to inelastic processes. This is probably because the electron-phonon coupling is not strong enough. In Fig. S3 within the Supplemental Material, we see that if the phonon energy is further reduced from the current value $\hbar\omega_0 = 0.085$ eV, the electron-phonon coupling and thus the inelastic processes are expected to increase by orders of magnitude. Another interesting observation here is that turning off elastic processes, counterintuitively, would significantly affect the TDDB process. On first thought, one would think that the elastic process does not involve phonons, thus it would not contribute to the heat power. It would then not affect the temperature distribution and the trap-generation process. However, we should keep in mind that TAT is a multistep (at least two-step) process. The electron tunneling into a trap and out of a trap are assumed to be two incoherent and independent processes. Also, current continuity should always be satisfied. Because of these reasons, it is well possible that while the first step is elastic, the next consecutive step is inelastic. One can think of an example trap site, which is within the inelastic processes difficult to capture an electron but easy to release an electron. If we take into account only inelastic process, the current density and heat power associated with this trap would be very low while if the elastic processes are introduced this trap might become a high-current and high-heat-power site. Another observation here is that if only the inelastic processes are taken into account, the trap-to-trap multistep processes now becomes

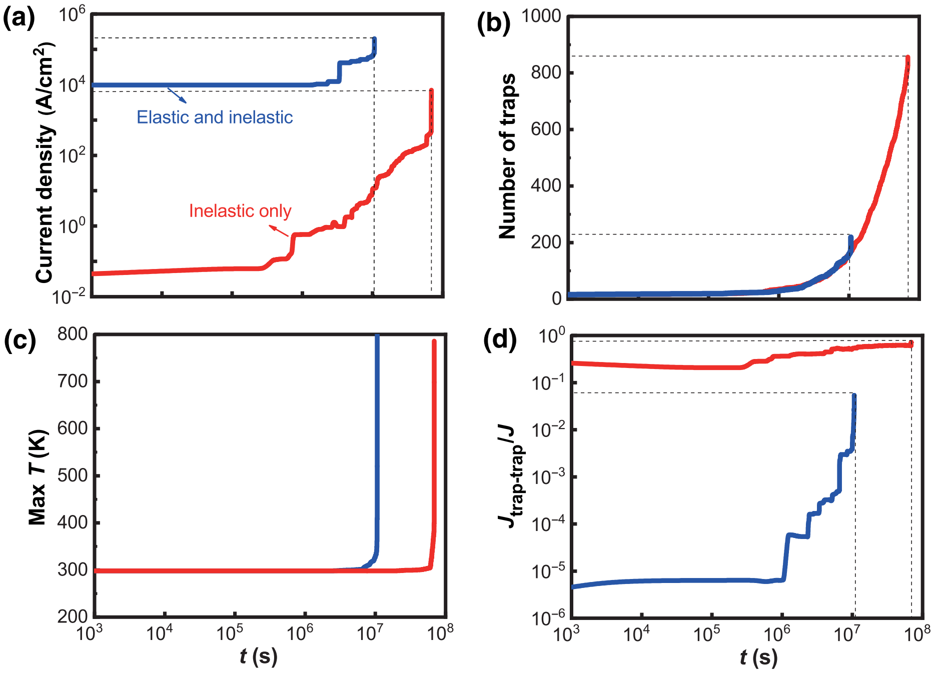

FIG. 13. Comparison between elastic+inelastic and inelastic-only cases. (a) Current density, (b) number of traps, (c) maximum temperature, and (d) the fraction of trap-to-trap current as a function of time during the TDDB process.

very significant. As shown in Fig. 13(d), the fraction of trap-to-trap current is $> 20\%$ even at the very beginning of TDDB, and approaches $> 80\%$ near the end. This again shows the relevance of our unique 3D master equation approach in this work, which accurately takes into account full 3D interactions of all trap sites.

IV. SUMMARY AND OUTLOOK

We present a 3D mechanistic model for the TDDB process in polycrystalline thin films. The model starts from microscopic description of trap states in the dielectric and the associated charge-transfer processes. By coupling 3D electric and thermal equations, the macroscopic polycrystalline system and its evolution towards dielectric breakdown are systematically depicted. The model calculation well reproduces experimental results and key material parameters are extracted. The modeling work also unravels significant physical insight during the TDDB process.

We also comment on the simulation speed of the model presented in this work. A typical simulation of the entire TDDB process with 400 traps generated in the end takes around 20 h on a standard up-to-date desktop computer. A single-step calculation of leakage current, temperature, and electric field takes a few minutes, which is repeated every time the trap number increases by 1. A larger device with 10^3 traps at breakdown can be calculated within 1 week.

The model could be further developed in the near future by improving the effective-mass-based semiclassical charge-transfer rates by first-principles calculations [26,51]. For example, the Miller-Abrahams hopping rate used in this work neglects lattice reorganization, which could play a significant role in the charge-trapping process associated with oxygen vacancies [52,53]. In our model, the traps are assumed to be static, i.e., they are fixed in position and chemically stable. However, it has been shown in the literature that the traps could be dynamic due to atomic migration during the TDDB process [54–56].

ACKNOWLEDGMENTS

This work is supported by the National Key R&D Program of China (No. 2021YFB3600601), the talents project of Guangdong Province, National Natural Science Foundation of China (No. 62005083, No. 12004119), Science and Technology Program of Guangzhou (No. 2019050001), Program for Guangdong Innovative and Enterpreneurial Teams (No. 2019BT02C241), Program for Chang Jiang Scholars and Innovative Research Teams in Universities (No. IRT 17R40), China Postdoctoral Science Foundation (No. 2020M672667), Natural Science Foundation of Guangdong Province (No. 2021A1515010623), Guangdong Provincial Key Laboratory of Optical Information Materials and Technology (No. 2017B030301007), Guangzhou Key Laboratory of Electronic Paper Displays Materials and Devices (No. 201705030007), MOE International Laboratory for Optical Information Technologies and the 111 Project.

[1] J. Suehle, Ultrathin gate oxide reliability: Physical models, statistics, and characterization, IEEE Trans. Electron Devices **49**, 958 (2002).
[2] A. Martin, P. O'Sullivan, and A. Mathewson, Dielectric reliability measurement methods: A review, Microelectron. Reliab. **38**, 37 (1998).
[3] F. Palumbo, C. Wen, S. Lombardo, S. Pazos, F. Aguirre, M. Eizenberg, F. Hui, and M. Lanza, A review on dielectric breakdown in thin dielectrics: Silicon dioxide, high-k, and layered dielectrics, Adv. Funct. Mater. **30**, 1900657 (2020).
[4] J. Verweij and J. Klootwijk, Dielectric breakdown I: A review of oxide breakdown, Microelectron. J. **27**, 611 (1996).
[5] J. H. Stathis, Reliability limits for the gate insulator in CMOS technology, IBM J. Res. Dev. **46**, 265 (2002).
[6] J. McPherson, Time dependent dielectric breakdown physics - models revisited, Microelectron. Reliab. **52**, 1753 (2012).
[7] R. Moazzami, J. Lee, and C. Hu, Temperature acceleration of time-dependent dielectric breakdown, IEEE Trans. Electron Devices **36**, 2462 (1989).
[8] J. W. McPherson and H. C. Mogul, Underlying physics of the thermochemical E model in describing low-field time-dependent dielectric breakdown in SiO_2 thin films, J. Appl. Phys. **84**, 1513 (1998).
[9] I.-C. Chen, S. Holland, and C. Hu, Electrical breakdown in thin gate and tunneling oxides, IEEE Trans. Electron Devices **32**, 413 (1985).
[10] K. F. Schuegraf and C. Hu, Reliability of thin SiO_2, Semicond. Sci. Technol. **9**, 989 (1994).
[11] D. J. DiMaria, E. Cartier, and D. Arnold, Impact ionization, trap creation, degradation, and breakdown in silicon dioxide films on silicon, J. Appl. Phys. **73**, 3367 (1993).
[12] D. J. DiMaria and J. W. Stasiak, Trap creation in silicon dioxide produced by hot electrons, J. Appl. Phys. **65**, 2342 (1989).
[13] J. Stathis, Physical and predictive models of ultrathin oxide reliability in CMOS devices and circuits, IEEE Trans. Device Mater. Reliab. **1**, 43 (2001).
[14] N. Suzumura, S. Yamamoto, D. Kodama, K. Makabe, J. Komori, E. Murakami, S. Maegawa, and K. Kubota, in *2006 IEEE Int. Reliab. Phys. Symp. Proc.* (2006), p. 484.
[15] J. Suñé, New physics-based analytic approach to the thin-oxide breakdown statistics, IEEE Electron Device Lett. **22**, 296 (2001).
[16] J. H. Stathis, Percolation models for gate oxide breakdown, J. Appl. Phys. **86**, 5757 (1999).
[17] R. Degraeve, G. Groeseneken, R. Bellens, J. Ogier, M. Depas, P. Roussel, and H. Maes, New insights in the relation between electron trap generation and the statistical properties of oxide breakdown, IEEE Trans. Electron Devices **45**, 904 (1998).
[18] L. Larcher, Statistical simulation of leakage currents in MOS and flash memory devices with a new multiphonon

trap-assisted tunneling model, IEEE Trans. Electron Devices **50**, 1246 (2003).

[19] G. Jegert, A. Kersch, W. Weinreich, and P. Lugli, Ultimate scaling of TiN/ZrO$_2$/TiN capacitors: Leakage currents and limitations due to electrode roughness, J. Appl. Phys. **109**, 014504 (2011).

[20] B. Weiler, T. Haeberle, A. Gagliardi, and P. Lugli, Kinetic Monte Carlo of transport processes in Al/AlO$_x$/Au-layers: Impact of defects, AIP Adv. **6**, 095112 (2016).

[21] G. Jegert, A. Kersch, W. Weinreich, U. Schröder, and P. Lugli, Modeling of leakage currents in high-k dielectrics: Three-dimensional approach via kinetic Monte Carlo, Appl. Phys. Lett. **96**, 062113 (2010).

[22] G. Jegert, A. Kersch, W. Weinreich, and P. Lugli, Monte Carlo simulation of leakage currents in TiN/ZrO$_2$/TiN capacitors, IEEE Trans. Electron Devices **58**, 327 (2011).

[23] L. Vandelli, A. Padovani, L. Larcher, and G. Bersuker, Microscopic modeling of electrical stress-induced breakdown in poly-crystalline hafnium oxide dielectrics, IEEE Electron Device Lett. **60**, 1754 (2013).

[24] L. Vandelli, A. Padovani, L. Larcher, R. G. Southwick, W. B. Knowlton, and G. Bersuker, A physical model of the temperature dependence of the current through SiO$_2$/HfO$_2$ stacks, IEEE Trans. Electron Devices **58**, 2878 (2011).

[25] L. Larcher, A. Padovani, and L. Vandelli, A simulation framework for modeling charge transport and degradation in high-k stacks, J. Comput. Electron. **12**, 658 (2013).

[26] A. Padovani, D. Z. Gao, A. L. Shluger, and L. Larcher, A microscopic mechanism of dielectric breakdown in SiO$_2$ films: An insight from multi-scale modeling, J. Appl. Phys. **121**, 155101 (2017).

[27] F. Liu, Y.-Y. Liu, L. Li, G. Zhou, X. Jiang, and J.-W. Luo, Three-Dimensional Mechanistic Modeling of Gate Leakage Current in High-κ MOSFETs, Phys. Rev. Appl. **13**, 024020 (2020).

[28] J. J. M. van der Holst, F. W. A. van Oost, R. Coehoorn, and P. A. Bobbert, Monte Carlo study of charge transport in organic sandwich-type single-carrier devices: Effects of Coulomb interactions, Phys. Rev. B **83**, 085206 (2011).

[29] T. Ando, N. D. Sathaye, K. V. R. M. Murali, and E. A. Cartier, On the electron and hole tunneling in a HfO$_2$ gate stack with extreme interfacial-layer scaling, IEEE Electron Device Lett. **32**, 865 (2011).

[30] J. Robertson and R. M. Wallace, High-k materials and metal gates for CMOS applications, Mater. Sci. Eng.: R: Rep. **88**, 1 (2015).

[31] Y.-C. Yeo, T.-J. King, and C. Hu, MOSFET gate leakage modeling and selection guide for alternative gate dielectrics based on leakage considerations, IEEE Trans. Electron Devices **50**, 1027 (2003).

[32] C. Hinkle, C. Fulton, R. Nemanich, and G. Lucovsky, A novel approach for determining the effective tunneling mass of electrons in HfO$_2$ and other high-K alternative gate dielectrics for advanced CMOS devices, Microelectron. Eng. **72**, 257 (2004).

[33] H. Allmaier, L. Chioncel, and E. Arrigoni, Titanium nitride: A correlated metal at the threshold of a Mott transition, Phys. Rev. B **79**, 235126 (2009).

[34] M. Ramzan, E. Ahmed, N. Niaz, A. Rana, A. Bhatti, N. Khalid, and M. Nadeem, AFM applications to study the morphology of HfO$_2$ multilayer thin films, Superlattices Microstruct. **82**, 399 (2015).

[35] J. Mcpherson, J. Y. Kim, A. Shanware, and H. Mogul, Thermochemical description of dielectric breakdown in high dielectric constant materials, Appl. Phys. Lett. **82**, 2121 (2003).

[36] G. Bersuker, Y. Jeon, and H. R. Huff, Degradation of thin oxides during electrical stress, Microelectron. Reliab. **41**, 1923 (2001).

[37] M. A. Panzer, M. Shandalov, J. A. Rowlette, Y. Oshima, Y. W. Chen, P. C. McIntyre, and K. E. Goodson, Thermal properties of ultrathin hafnium oxide gate dielectric films, IEEE Electron Device Lett. **30**, 1269 (2009).

[38] K. McKenna and A. Shluger, The interaction of oxygen vacancies with grain boundaries in monoclinic HfO$_2$, Appl. Phys. Lett. **95**, 222111 (2009).

[39] S. Unnikrishnakurup, C. V. Krishnamurthy, and K. Balasubramaniam, in *Quantitative InfraRed Thermography* (2015).

[40] N. Raghavan, K. L. Pey, K. Shubhakar, and M. Bosman, Modified percolation model for polycrystalline high-κ gate stack with grain boundary defects, IEEE Electron Device Lett. **32**, 78 (2011).

[41] G. Bersuker, J. Yum, L. Vandelli, A. Padovani, L. Larcher, V. Iglesias, M. Porti, M. Nafría, K. McKenna, A. Shluger, P. Kirsch, and R. Jammy, Grain boundary-driven leakage path formation in HfO$_2$ dielectrics, Solid State Electron. **65–66**, 146 (2011).

[42] J. E. Medvedeva, Averaging of the electron effective mass in multicomponent transparent conducting oxides, Europhys. Lett. **78**, 57004 (2007).

[43] M. Herrmann and A. Schenk, Field and high-temperature dependence of the long term charge loss in erasable programmable read only memories: Measurements and modeling, J. Appl. Phys. **77**, 4522 (1995).

[44] A. Miller and E. Abrahams, Impurity conduction at low concentrations, Phys. Rev. **120**, 745 (1960).

[45] J. Blumberger and K. P. McKenna, Constrained density functional theory applied to electron tunnelling between defects in MgO, Phys. Chem. Chem. Phys. **15**, 2184 (2013).

[46] K. McKenna and J. Blumberger, First principles modeling of electron tunneling between defects in m-HfO$_2$, Microelectron. Eng. **147**, 235 (2015).

[47] R. Tsu and L. Esaki, Tunneling in a finite superlattice, Appl. Phys. Lett. **22**, 562 (1973).

[48] See the Supplemental Material at http://link.aps.org/supplemental/10.1103/PhysRevApplied.19.024008 for additional discussions on steady-state heat transport, thermal insulating grain boundaries, and effect of trap recombination, phonon energy, bond polarizability, and grain properties on TDDB.

[49] A.-M. El-Sayed, M. B. Watkins, T. Grasser, and A. L. Shluger, Effect of electric field on migration of defects in oxides: Vacancies and interstitials in bulk MgO, Phys. Rev. B **98**, 064102 (2018).

[50] J. Strand, P. La Torraca, A. Padovani, L. Larcher, and A. L. Shluger, Dielectric breakdown in HfO$_2$ dielectrics: Using multiscale modeling to identify the critical physical processes involved in oxide degradation, J. Appl. Phys. **131**, 234501 (2022).

[51] Y.-Y. Liu, F. Liu, R. Wang, J.-W. Luo, X. Jiang, R. Huang, S.-S. Li, and L.-W. Wang, Characterizing the Charge Trapping across Crystalline and Amorphous Si/SiO_2/HfO_2 Stacks from First-Principle Calculations, Phys. Rev. Appl. **12**, 064012 (2019).

[52] C. Schleich, D. Waldhör, T. Knobloch, W. Zhou, B. Stampfer, J. Michl, M. Waltl, and T. Grasser, Single- versus multi-step trap assisted tunneling currents—part i: Theory, IEEE Trans. Electron Devices **69**, 4479 (2022).

[53] C. Schleich, D. Waldhör, A.-M. El-Sayed, K. Tselios, B. Kaczer, T. Grasser, and M. Waltl, Single- versus multi-step trap assisted tunneling currents—part ii: The role of polarons, IEEE Trans. Electron Devices **69**, 4486 (2022).

[54] T. V. Zaporozhets, A. M. Gusak, K. N. Tu, and S. G. Mhaisalkar, Three-dimensional simulation of void migration at the interface between thin metallic film and dielectric under electromigration, J. Appl. Phys. **98**, 103508 (2005).

[55] Y. Li, P. Huang, S. Di, X. Zhang, G. Du, and X. Liu, Comprehensive investigation of multitraps-induced degradation in HfO_2-based nmosfets with interfacial layer by three-dimensional KMC method, IEEE Trans. Nanotechnol. **17**, 198 (2018).

[56] Y. Li, H. Jiang, Z. Lun, Y. Wang, P. Huang, H. Hao, G. Du, X. Zhang, and X. Liu, Reliability investigation of high-k/metal gate in nMOSFETs by three-dimensional kinetic Monte-Carlo simulation with multiple trap interactions, Jpn. J. Appl. Phys. **55**, 04ED15 (2016).